SAND99-0581C

Interferometric measurement for improved understanding of boundary effects in micromachined beams

Brian D. Jensen*, Fernando Bitsie, and Maarten de Boer

Sandia National Laboratories
Albuquerque, NM, USA
http://www.mdl.sandia.gov/Micromachine

ABSTRACT

Micromachined beams are commonly used to measure material properties in MEMS. Such measurements are complicated by the fact that boundary effects at the ends of the beams have a significant effect on the properties being measured. In an effort to improve the accuracy and resolution of such measurements, we are conducting a study of support post compliances in cantilever and fixed-fixed beams. Three different support post designs have been analyzed by finite element modeling. The results are then compared to measurements made on actual devices using interferometry. Using this technique, the accuracy of measurements of Young's modulus has been improved. Continuing work will also improve the measurement of residual stress.

Keywords: material properties, step-up anchor, surface micromachining, interferometry

1. INTRODUCTION

Micromachined beams are commonly used for the extraction of material properties in MEMS. For example, cantilever beams have been used to measure curvature resulting from a strain gradient [1-3] as well as Young's modulus [3]. A number of researchers have also used fixed-fixed beams to measure residual stress [1-7]. Most of these researchers have concluded that boundary conditions at the beam ends significantly affect the accuracy of the measurements.

We have recently proposed a new technique for measuring the material properties listed above [8]. This technique, called IMaP (Interferometry for Material Properties), relies on point-by-point deflection curves of actuated beams measured using interferometry. The beams may be either unloaded or pulled toward the substrate by electrostatic forces. The beam deflection curves are then compared to deflection models to find the values of material properties which minimize error between the measured and modeled deflections. Because the interferometry system yields high-resolution data (within about 10 nm), the material properties can be measured very accurately. In addition, because the measurements are not destructive, a single beam can be used to generate a large amount of data, reducing the chip area required for the test devices. Moreover, because measured and modeled deflections are matched along the entire length of the beam rather than at only one point, high confidence is obtained in the measured property values. These high-confidence, high-resolution material property measurements allow better process control and design optimization.

Because the boundary effects change the global beam deflections, they must be modeled to obtain accurate material property measurements. We have previously modeled the beam support post as a short cantilever beam subjected to forces and moments resulting from the long beam's deflection, similar to the presentation in [9]. Because of the difficulty of accurately measuring the boundary conditions (such as the beam end angle), the work in [9] included extensive finite element analysis but no experimental data. Work has also been presented on designing stiffer support posts [10], although no associated simple model was presented. However, several of the boundary effects can be measured using IMaP. Therefore, we have begun a study of the boundary effects of micromachined beams. Using finite element modeling in conjunction with experimental measurements, the strengths and weaknesses of our proposed model have been identified, and a more accurate model has been developed. This paper discusses the results which have been gathered to this time. This introduction describes background material, and the following sections describe the experiments which have been performed.

*Correspondence: Email: bjense@sandia.gov; Internet: http://www.mdl.sandia.gov/Micromachine; Tel.: (505)844-7465; Fax: (505)844-2991

DISCLAIMER

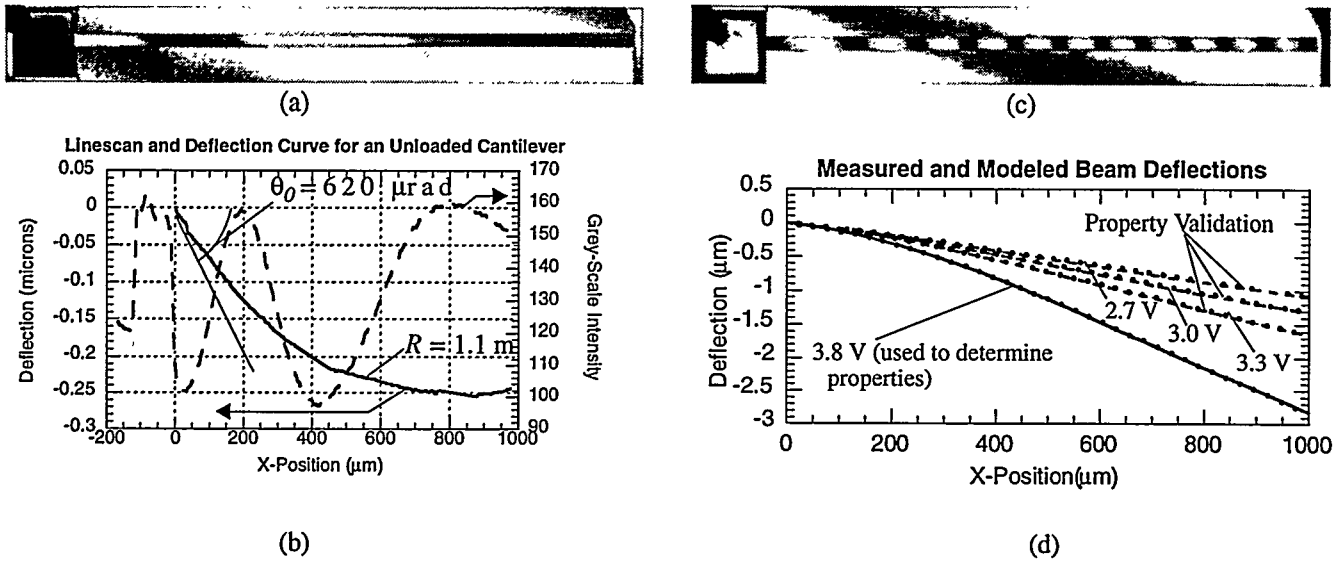

Figure 1: Interferograms of a 1,000 µm long cantilever. (a) is unloaded, with the corresponding deflection curve shown in (b). (c) shows the beam loaded at 3.8V, with the corresponding deflection and deflections at other voltages shown in (d). Dots show measured curves, and lines show modeled curves in (d).

1.1 A brief description of IMaP

Both cantilever and fixed-fixed beams are used in the IMaP methodology. The measurement process consists of four steps, each of which measures a different property [8]. First, either multi-wavelength interferometry or profilometry is used to measure the thickness of the film being studied as well as the gap between the beams and the underlying electrodes. Either method has very good resolution, with the error being 20 nm or less. This high resolution ensures the accuracy of the model. Next, the deflection of an unloaded cantilever beam is measured using interferometry, as shown in Figure 1a. The resulting accurate deflection curve, shown in Figure 1b, is compared to a model to find the values for unloaded beam end angle and film curvature which minimize error between the model and the measurement. In the case shown here, the beam end angle θ_0 is 620 µrad, with a radius of curvature R of 1.1 m. Next, the deflection of a cantilever beam pulled toward the substrate with electrostatic forces is measured, as shown in Figure 1c. Modeling the deflection allows determination of the elastic modulus (Young's modulus) of the material as well as the compliance of the support post. In this case, Young's modulus is 169 GPa, and the support post compliance is 3.2 µrad/µN•µm. These results were verified by measuring deflection at other voltages, as shown in Figure 1d. In this figure, dots represent measured data, and lines represent modeled data. Finally, the deflection curve of a loaded fixed-fixed beam allows extraction of the film's residual stress. Figure 2 shows a fixed-fixed beam with a measured residual stress of 2.9 MPa, in compression.

1.2 Support Post Modeling

Classical beam mechanics treats the boundaries of cantilever and fixed-fixed beams as completely fixed - that is, the deflection and slope of the beam at the boundary are both zero, regardless of the loads applied. Actual beam boundaries do not exhibit this behavior - the deflection and slope of the beam at the support post change with applied load. This section describes the existing model used to predict support post non-idealities.

We have previously modeled the support post as a short cantilever beam, as shown in Figure 3. The end of the beam applies a moment M and a force load F to the support post, causing it to deform. In addition, the support post may have an unloaded deformation due to residual stress in the post itself. The support post deformation may be broken into two parts which affect IMaP measurements - the beam end angle and the beam axial deflection, denoted θ and δ. As shown in the figure, each type of deformation has an initial (unloaded) value, a component due to the applied moment, and a component due to the applied force. For an equivalent cantilever beam of length L_{sp} and cross-sectional moment of inertia I_{sp}, small-deflection beam mechanics gives

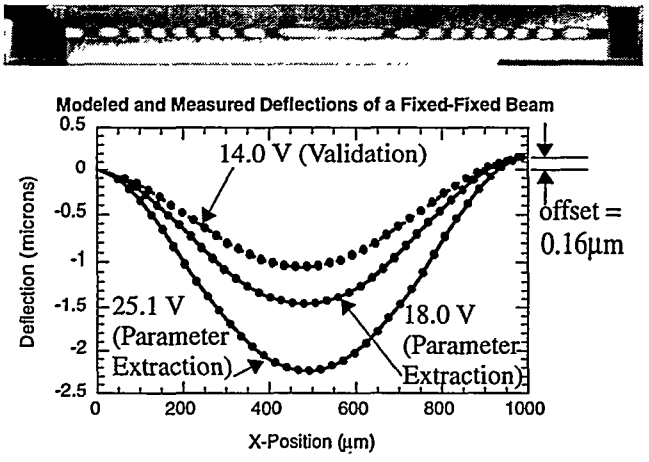

Figure 2: Interferogram and deflection curves for a 1,000 µm fixed-fixed beam. Dots show measured data; lines show modeled curves.

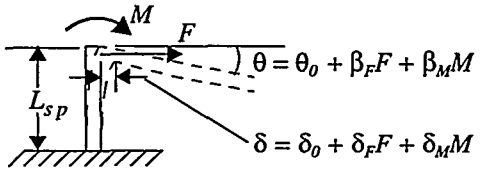

Figure 3: The beam support post model

$$\theta = \theta_0 + \frac{FL_{sp}^2}{2EI_{sp}} + \frac{ML_{sp}}{EI_{sp}} = \theta_0 + \beta_F F + \beta_M M \tag{1}$$

and

$$\delta = \delta_0 + \frac{FL_{sp}^3}{3EI_{sp}} + \frac{ML_{sp}^2}{2EI_{sp}} = \delta_0 + \delta_F F + \delta_M M \tag{2}$$

where E is Young's modulus. Thus, according to this model, β_F, β_M, δ_F, and δ_M from Figure 3 may all be determined if the geometry of the associated cantilever beam is known. This model, which assumes an equivalent cantilever for both angular and axial beam deflections, will subsequently be called model 1.

It should be noted that while θ_0 has been measured on multiple beams [1, 8], δ_0 has never been measured, as its size (a few nanometers) is too small for most measurement techniques. Its presence is being suggested here for the first time. However, it is reasonable to suppose that such a phenomenon exists because of the proven existence of an unloaded angular deflection at the support post.

No axial force exists in a cantilever beam pulled toward the substrate, so the effects of the axial force may be ignored for cantilever beams. In addition, δ, which is typically on the order of a few nanometers, does not significantly affect the beam's deflection. Therefore, for cantilever beams, only θ_0 and β_M are significant factors. However, a fixed-fixed beam has an axial force and an end moment, requiring the consideration of all six factors. This is because even nanometer-scale deflections can affect the apparent stress in the beam by up to a few MPa, depending on the length of the beam. For example, if δ is 1 nm for a 300 µm polysilicon fixed-fixed beam, the induced stress is equal to

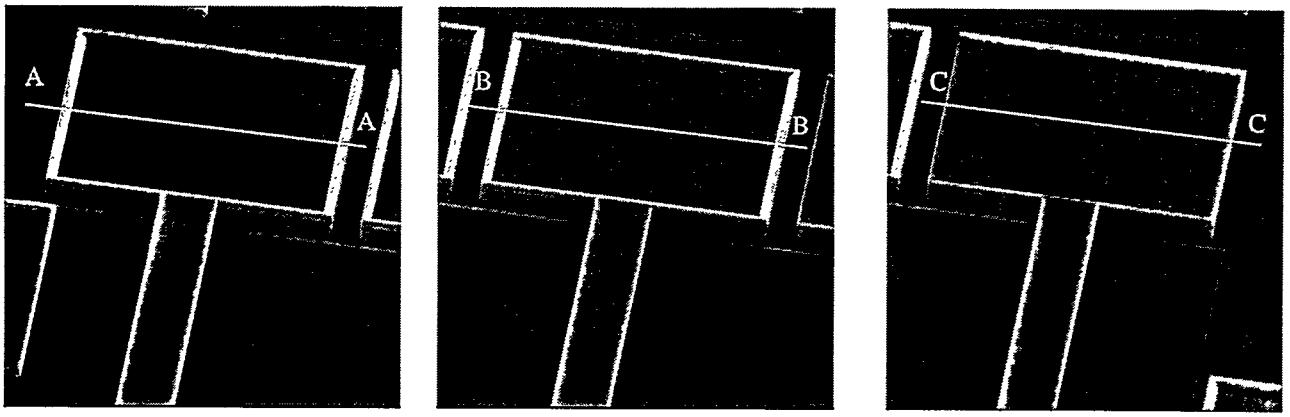

(a) (b) (c)

Figure 4: SEM micrographs of each support pad design. (a) shows Pad 1, the most compliant pad. (b) is Pad 2, with intermediate compliance, and (c) is Pad 3, which is the stiffest pad design.

$$\sigma = \frac{2\delta E}{L} = 1.12 \text{ MPa} \tag{3}$$

for E = 168 GPa. This effect may be as much as the as-fabricated residual stress for good-quality polysilicon.

2. EXPERIMENTAL APPROACH

To measure the effectiveness of model 1, the deformations of three different support post designs were studied. Each pad design was analyzed by the finite element method. Cantilever and fixed-fixed beams using each support post design were also fabricated in SUMMiT, Sandia's four-level polysilicon surface micromachining process. Three beam lengths (300, 500, and 700 μm) were fabricated for each support post design to allow a range of loads to be applied, with the longer beams generally applying smaller loads to the boundaries because of their reduced stiffness. Interferometric measurements of the beams' deflections allowed independent extraction of beam end angle as well as material properties. By comparing the initial results for beam end angle from the deflection of several beams, more accurate model parameters for support post compliance in each pad design were calculated. We then repeated analysis of the beam deflection data, allowing only the material property of interest to vary in finding the best modeled fit to the data. In this second analysis, we used the model parameters developed from the first analysis to determine beam end angle. The resulting measurement of material properties was more accurate than the measurement made only using the first analysis.

This section describes each support post design, and the following section describes the finite element modeling of each support post. Subsequent sections describe the experimental testing of cantilever and fixed-fixed beams.

2.1 Support post designs

Each support post was designed to support a beam fabricated in the top layer of polysilicon. SEM micrographs of each support are shown in Figure 4. Figure 5 shows cross-sections of each pad design taken at the cross-section lines shown in Figure 4. Because each beam is fabricated in the top layer of polysilicon, the support post must build up to that layer using an underlying layer. Pad 1 is created by cutting the oxide under the underlying layer across the whole field of the support pad. The oxide which separates the two polysilicon layers is partially removed across the whole area, although some oxide remains trapped between the two layers. The result is a step-up support post, as is generally seen for surface-micromachined beams.

Pad 2 is created by making long, narrow cuts in the lowest oxide layer. These long cuts are almost completely filled in by the first polysilicon layer. In addition, the oxide which is not removed (between the narrow cuts) is trapped so that it is not etched during the release, resulting in a fairly stiff structure. The oxide layer which separates the polysilicon layer is then completely removed across the area of the pad, resulting in a step-up which is not as high as the step in Pad 1, reducing its compliance somewhat. Note that in the direction orthogonal to the cross-section, the lower layer would either have a long stretch of polysilicon or a long area of entrapped oxide, depending on whether the cross-section was made at an oxide cut or not.

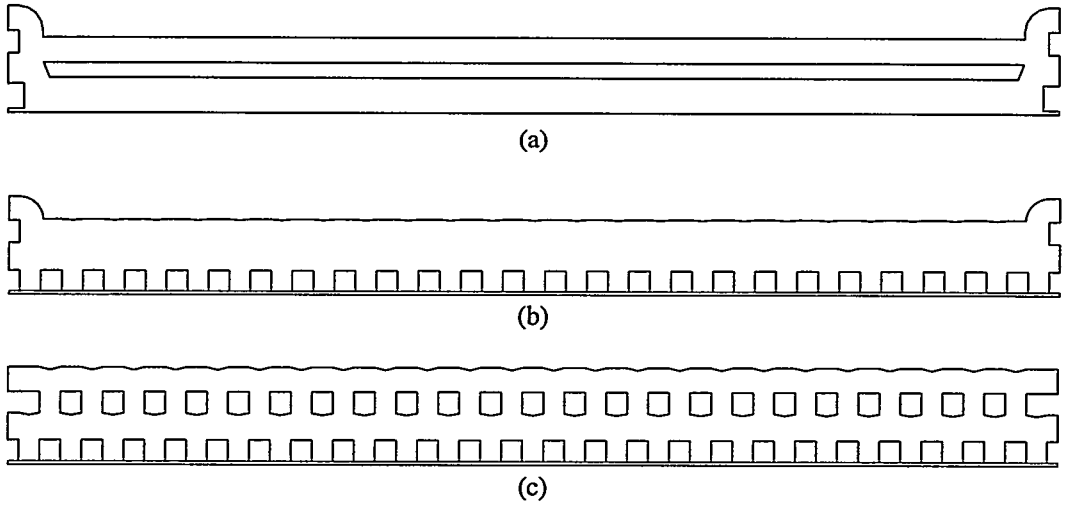

Figure 5: Cross-sections of each support pad design. (a) is Pad 1, taken through line A-A in Figure 4a. (b) is Pad 2, taken through line B-B in Figure 4b, and (c) is Pad 3, taken through line C-C in Figure 4c. The holes represent trapped oxide. Pad 1 is the most compliant, Pad 2 has intermediate compliance, and Pad 3 is the stiffest.

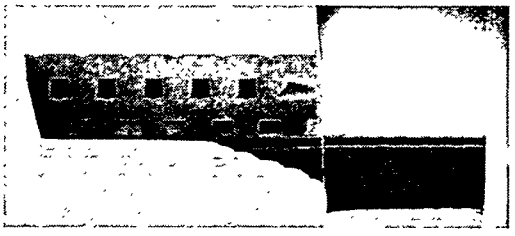

Figure 6: A Focused Ion Beam (FIB) cross-section of Pad 3, showing the oxide trapped inside the pad.

Pad 3 is created using staggered long, narrow cuts in both oxide layers. As a result, there is no step-up at the connection to the beam, as Figure 4c shows. The absence of a step causes this pad to be the stiffest of the three. Figure 6 shows a Focused Ion Beam (FIB) cross-section of the pad, with the trapped oxide plainly visible as the dark squares within the polysilicon pad.

3. FINITE ELEMENT MODELING

Finite element modeling was used to predict the stiffness of each pad. This section describes the finite element modeling and presents the results of the modeling.

3.1 Modeling

A 3D solid model was generated to represent each pad design. These solid models are shown in Figure 7. Because of symmetry, only half of each support pad was modeled, with the line of symmetry occurring at the center of the beam. In addition, early solutions showed that parts of the pad far away from the beam connection had no effect on the deformation, so only the area of the pad less than 40 μm from the beam was modeled. Also, although oxide was trapped in several places in the actual pads, the oxide was ignored in the solid models because earlier results had shown the oxide to have only a small effect. The solid models were meshed with brick elements.

3.2 Loading

To find the deformation of the pads due to beam axial forces and end moments, loads were applied to the beam connection areas of each pad design. A force of 100 μN acting along the direction of the beam simulated a beam axial force. A moment was applied using a force couple of 45 μN acting on both the top and bottom of the beam connection area. Based on the measured film thickness of 2.28 μm, this represents a moment load of 102.6 μN•μm. These loads were chosen to be in the range of the

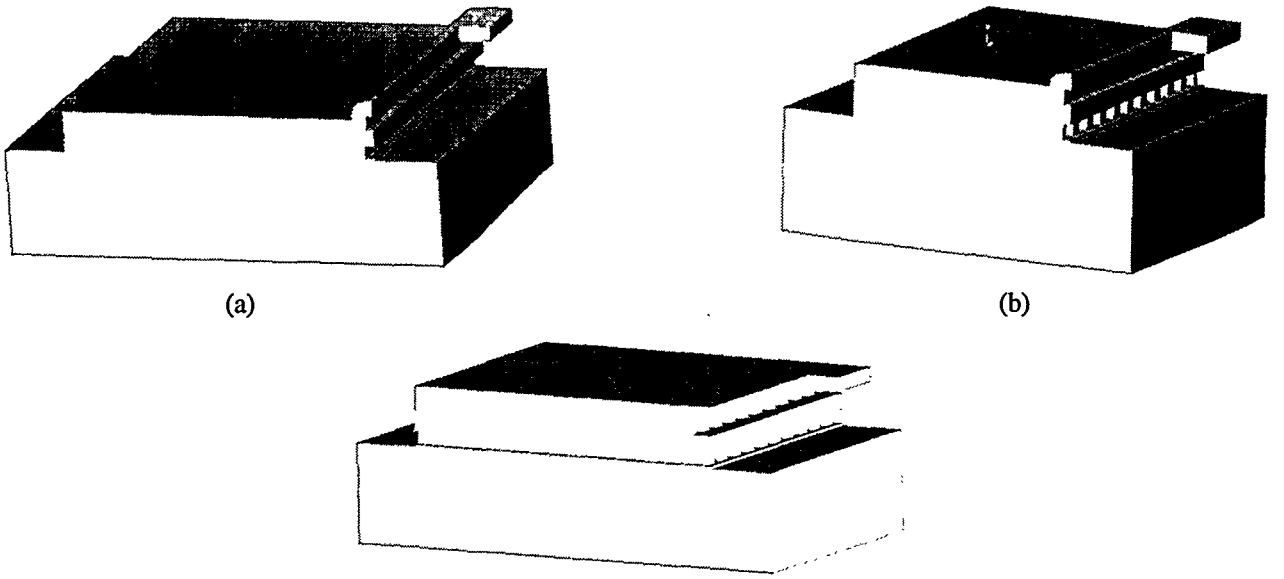

Figure 7: Solid models for Pad 1 (a), Pad 2 (b), and Pad 3 (c).

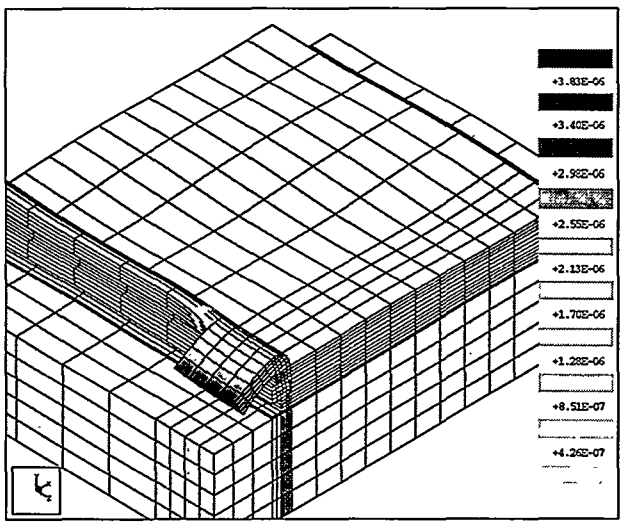

Figure 8: Deflection of Pad 1 under a horizontal force of 100 mN and a moment of 102.6 mN•mm. The deflection is amplified 1,000 times to make it easy to see.

actual loads expected during testing. The finite element solution was found using the solver ProMechanica with a linear model. A sample deflection solution for Pad 1 is shown in Figure 8.

We expect the deformation of the pads to be linear with respect to the loads over the range of actual loading. To test this, solutions were found using Pad 3 for applied loads 3, 10, and 30 times those described in the preceding paragraph. Figure 9 shows the response of θ and δ to each load level, indicating a high degree of linearity over a wide range. Actual loads expected during testing are not more than 10 times the initial load. Because of the high degree of linearity for Pad 3, the other two pad designs are also expected to have a highly linear response.

3.3 Results of FEM

Because of the linear response of the support pads, a single solution allows extraction of the lumped parameters β_F, β_M, δ_F, and δ_M defined in Figure 3. This is done simply by finding the θ or δ due to each load and then dividing by the value of the load. The results for each pad are listed in Table 1.

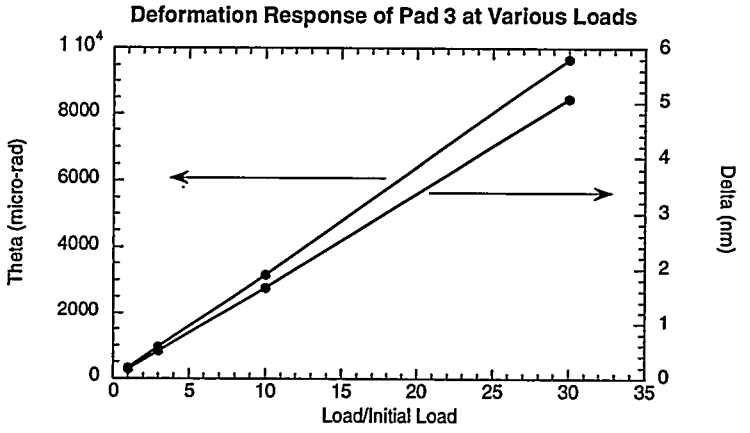

Figure 9: Linearity of deformation for Pad 3.

The results show that for each case except one, the support pads have the expected relative compliances, with Pad 1 the most compliant, Pad 2 of intermediate compliance, and Pad 3 the least compliant. β_F, δ_F, and δ_M all show this effect. However, β_M does not show this effect; in fact, the three pad designs are almost equally compliant with respect to angular deflection caused by a moment. This is probably because each pad includes an overhang at the beam connection; this overhang is required by the design rules to ensure that the polysilicon completely surrounds all oxide cuts. Apparently, the majority of the angular deflection due to moment results from this overhang, which is identical in each pad design.

The finite element results immediately point to a problem in model 1. Recall from Equations (1) and (2) that the model indicates that everything about the pad is known if the equivalent length L_{sp} and cross-sectional moment of inertia I_{sp} are known. If L_θ and L_δ are defined as the equivalent support post cantilever lengths found using the θ's and δ's, respectively, then

$$L_\theta = 2\frac{\beta_F}{\beta_M} \tag{4}$$

and

$$L_\delta = \frac{3\delta_F}{2\delta_M} \tag{5}$$

which are derived from Equations (1) and (2). If model 1 is correct, then these two equivalent lengths should be equal. The solutions to Equations (4) and (5) are shown in Table 2. The results clearly indicate that the effective support post beam lengths are not the same for angular and axial deflections, so that different model parameters must be used in each case. This means that model 1 is inadequate to completely express the stiffness of the support posts with respect to both angular and axial deflection of the beam ends. The inadequacy most likely arises because we are trying to describe very complex support post designs as simple cantilever beams. The FEM results show that such a description is not appropriate. Instead, model 2 is proposed. This model uses the same conceptual picture presented in Figure 3, but does not require the support post cantilever to be the same

Table 1: Results of the finite element modeling.

	β_F (μrad/μN)	β_M (μrad/μN•μm)	δ_F (nm/μN)	δ_M (nm/μN•μm)
Pad 1	1.47	2.73	0.00475	0.00302
Pad2	0.89	2.47	0.00300	0.00175
Pad3	0.22	2.60	0.00150	0.00039

for both angular and axial deflections. This model was tested by studying support post effects on fixed-fixed beams, as will be discussed later in this paper.

4. CANTILEVER BEAM MEASUREMENTS

Our next step in characterizing the three pad designs was to measure the deflections of the cantilever beams to find the film radius of curvature R, the initial (unloaded) beam end angle θ_0 associated with each pad design, the support post compliance β_M of each support post design, and Young's modulus E. This section describes the analysis of the cantilever beams. The data will demonstrate how the accurate modeling of the support posts led to improved accuracy in measuring Young's modulus.

4.1 Measurement of radius of curvature and unloaded beam end angle

Profilometry measurements of the chips indicated a film thickness of 2.28 μm, with a gap of 6.62 μm between the beams and the electrodes. Based on these results, the beam end angle θ_0 and film radius of curvature R were found using the measured deflection curves of unloaded cantilever beams. Because the beams are fairly flat, only the 700 μm beams were long enough to make a good measurement of curvature. The results for each 700 μm beam are shown in Table 3, where positive angles represent bending toward the substrate. Each pad design has a different unloaded angle θ_0, but the radii correspond well because all of the beams are created from the same level of polysilicon. The average radius of curvature based on all three beams is 282 μm.

4.2 Measurement of support post compliance and Young's modulus

Using interferometry, the deflection curves of each cantilever were found at a various voltage loads. The values for E and β_M were then found which minimized error between the modeled and measured deflections. In this initial analysis, both E and β_M were allowed to vary to find the best possible fit to the measured deflections. Error was measured as RMS error per measured data point. Based on these results, a plot of the beam end moment versus beam end angle was generated. The plot, shown in Figure 10, shows good agreement with the FEM results, and verifies the linear response of the bond pads. In addition, the data shows a natural separation between the three pad designs due to the different unloaded angles of each pad. These initial angles must be measured in this way because FEM does not predict it. The linear regression fits shown plotted have equations of:

$$\begin{array}{lll} \text{Pad 1} & \theta = 790.9 + 2.24M & r^2 = 0.9281 \\ \text{Pad 2} & \theta = -98.1 + 2.35M & r^2 = 0.7213 \\ \text{Pad 3} & \theta = 294.7 + 2.26M & r^2 = 0.9360 \end{array} \quad (6)$$

Table 2: Equivalent support post beam lengths based on beam end angle and axial deflection.

	L_θ, μm	L_δ, μm
Pad 1	1.08	2.36
Pad 2	0.72	2.57
Pad 3	0.17	5.77

Table 3: Unloaded initial angle and curvature measured on each unloaded 700 μm cantilever.

	θ_0, μrad	R, mm
Pad 1	910	267
Pad 2	10	274
Pad 3	590	305

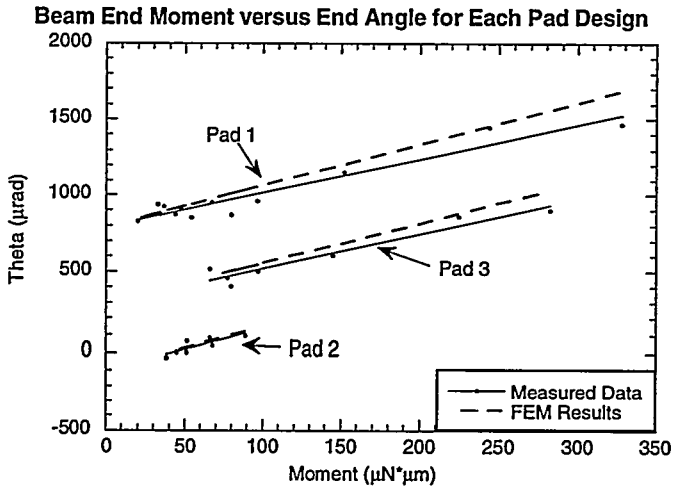

Figure 10: Beam end angle plotted against beam end moment for all cantilever beams. The best fit for measured slope (solid lines) corresponds well with the FEM predictions.

where r^2 is the correlation coefficient. In these equations, the first number is θ_0, and the second number is β_M. Each parameter shows fairly good agreement with the measured values from Table 3 and the modeled values from Table 1, respectively. Differences in θ_0 are most likely due to better measured data at the larger deflections represented in Figure 10 compared to the small unloaded deflections, while differences in β_M are most likely due to assumptions made during FEM, such as ignoring the effect of the oxide.

Using Equation (6) as a model for support post compliance allowed a better measurement of Young's modulus to be made. In generating the results shown in Figure 10, both beam end angle and Young's modulus were allowed to vary to find the best fit. The result was a relatively large amount of spread Young's modulus, as shown in Table 4. In addition, the mean Young's moduli for each pad design do not agree. Therefore, after processing this data and generating the linear fits found in Equation (6), the analysis was repeated. In this second analysis, beam end angle was not free to vary, but was given by Equation (6). The effect of this change is to incorporate modeling of the support post compliance directly into the beam deflection model, so that Young's modulus is the only remaining variable. It is then found by determining the value which minimizes the error between the measured deflection and the modeled deflection. The results of this second analysis are much more consistent across the different pad designs, and the overall coefficient of variation decreased by nearly a factor of three. Thus, non-systematic errors in measurement are reduced.

5. FIXED-FIXED BEAM MEASUREMENTS

The support post deformations in fixed-fixed beams are much more complicated than those for cantilever beams. This is because both axial forces and end moments act in the beam, and both beam end angle θ as well as beam end deflection δ must be considered. In particular, as δ is generally quite small (on the order of a few nanometers), it has not been effectively measured, which makes independent validation of the modeling impossible at present. The results reported here will show that model 2 performs well; however, based on the assumption that the residual stress is the same on separate beams in close proximity, better modeling is necessary before the support post behavior at fixed-fixed beams can be fully understood.

Table 4: Means and variation in Young's modulus for the two different types of analysis. All values are given in GPa, except for the coefficient of variation.

	Pad 1 Mean	Pad 2 Mean	Pad 3 Mean	Overall Mean	Overall St. Dev.	CV
Analysis allowing E and θ to vary	150	151	157	152	4.9	3.2%
Analysis modeling θ and allowing E to vary	156	156	157	156	1.9	1.2%

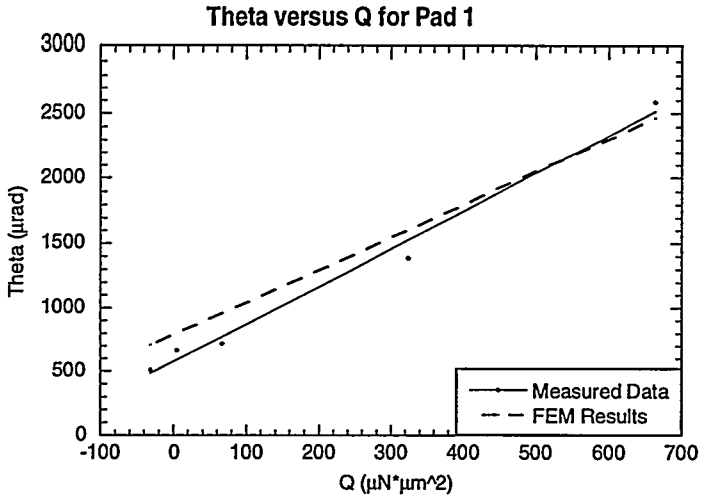

Figure 11: θ versus Q for Pad 1 fixed-fixed beams. The dashed line represents FEM results; the solid line is the linear regression fit for the measured data.

5.1 Extraction of residual stress and fixed-fixed beam support post compliance

Each of the fixed-fixed beams in the study was actuated under several different voltages, and the corresponding deflection curves were measured. The best values of beam end angle and residual stress were then found to match the measured and modeled deflections. As with the cantilever beams, in this first analysis both beam end angle and residual stress were allowed to vary in order to find the best possible fit. The beam end forces and moments for each beam deflection were also recorded. We combined the end loads into a single lumped parameter Q which reflects the simultaneous loading of both axial forces and bending moments. Q is found according to the equation

$$Q = \frac{FL_\beta^2}{2} + ML_\beta \tag{7}$$

so that Equation (1) may be written

$$\theta = \theta_0 + \frac{Q}{EI} \tag{8}$$

In Equation (7), L_β from Table 2 was used for each pad design. The beam end angle was then plotted against Q. An example plot for Pad 1 is shown in Figure 11. Each of the other pads showed a similar degree of linearity and similarity to the FEM data. The equations for the linear regression fits are:

$$\begin{array}{lll} \text{Pad 1} & \theta = 575.0 + 3.16M + 1.70F & r^2 = 0.9888 \\ \text{Pad 2} & \theta = 95.7 + 1.63M + 0.59F & r^2 = 0.8290 \\ \text{Pad 3} & \theta = 207.1 + 1.88M + 0.16F & r^2 = 0.7193 \end{array} \tag{9}$$

where θ is in units of µrad, and the moments must be in units of µN•µm, and the forces in units of µN.

Unfortunately, despite the relatively good fit, indicated by the fairly high correlation coefficients, the factors reflected in Equation (9) do not correlate very well with the corresponding FEM results listed in Table 1. Even though the agreement was not as good as desired, though, the data was re-analyzed, as with the cantilever beams, to improve the measurement of residual stress. With this second analysis, instead of allowing θ to vary, the factors in Equation (9) were used to model θ, and the best associated value of residual stress, σ_R, was then found for each deflection curve. In addition, for each analysis, δ_0, as defined in Figure 1, was optimized to find the value which minimized the differences in residual stress between measurements taken for the same pad design. The total axial deflection δ was calculated using Equation (2), and using L_δ for L_{sp}. The data for the first

Table 5: Residual stress measured in the fixed-fixed beams. All values are given in terms of MPa. All mean stresses are compressive.

	Pad 1 Mean	Pad 1 St. Dev.	Pad 2 Mean	Pad 2 St. Dev.	Pad 3 Mean	Pad 3 St. Dev.	Overall Mean	Overall St. Dev.
Analysis allowing σ_R and θ to vary	5.7	0.90	0.28	1.59	0.63	0.55	1.58	2.42
Analysis modeling θ and allowing σ_R to vary	3.9	0.12	2.24	0.63	1.53	0.15	2.24	1.01

and second analyses is presented in Table 5. The second analysis shows significantly less variability than the first, but it is still not as good as we expect to achieve. In particular, as we assume consistent residual stress in each beam, each pad design should yield the same residual stress result. Therefore, we conclude that model 2 is not as effective as we would like. We are continuing to do research in this area to improve the models, leading to better measurements of residual stress.

6. CONCLUSION

FEM and interferometric measurements have been used to investigate a simple model for support post compliance in micromachined beams. Three different support post designs were investigated to examine the robustness of the models. Experimental data showed that each support pad design had different initial undeflected angles, and FEM showed that each pad had different stiffnesses. In addition, FEM showed that the models previously suggested in [8] and [9] are insufficient to describe both angular and axial deflections at the beams' ends. Instead, a new model was suggested which treats angular and axial deflections separately. This model described some of the effects, but failed to produce the desired understanding of boundary effects in fixed-fixed beams.

The results showed a good understanding of effects in cantilever support posts, leading to improved accuracy of Young's modulus measurements using the IMaP methodology. Results for fixed-fixed beams showed more variation in the measurement of residual stress, and, consequently, less confidence. Work is underway to improve our understanding of fixed-fixed beam support post compliance. This work will significantly improve the accuracy of material properties measurements, leading to better process control and design optimization.

ACKNOWLEDGMENTS

The skills of Daniel Gutierrez in gathering the interferometry data, Gary Zender in taking the SEM micrographs, and Alex Pimentel in taking the FIB cross-section are gratefully acknowledged. We also acknowledge the Microelectronics Development Laboratory as Sandia National Laboratories for the fabrication of the devices investigated. Sandia is a multiprogram laboratory operated by Sandia Corporation, a Lockheed Martin Company, for the United States Department of Energy under contract DE-AC04-94AL85000.

REFERENCES

[1] Lober, T.A., Huang, J., Schmidt, M.A., and Senturia, S.D., "Characterization of the Mechanisms Producing Bending Moments in Polysilicon Micro-Cantilever Beams by Interferometric Deflection Measurements," *Hilton Head*, pp. 92-95, Hilton Head Island, South Carolina, 1988.

[2] Fang, W., Hu, H., and Lee, C.-H., "Design Criteria for Buckling Microbridges," *SPIE Conference on Micromachining and Microfabrication Process Technology IV*, SPIE Vol. 3511, pp. 288-296, Santa Clara, California, 1998.

[3] Osterberg, P.M. and Senturia, S.D., "M-TEST: A Test Chip for MEMS Material Property Measurement Using Electrostatically Actuated Test Structures," *J. Microelectromechanical Systems*, 6(2), pp. 107-118, June 1997.

[4] Lin, S.C.H. and Pugacz-Muraszkiewicz, I., "Local Stress Measurement in Thin Thermal SiO_2 Films on Si Substrates," *J. Applied Physics*, 43(1), pp. 119-125, January 1972.

[5] Guckel, H., Burns, D., Rutigliano, C., Lovell, E., and Choi, B., "Diagnostic microstructures for the measurement of intrinsic strain in thin films," *J. Micromech. Microeng.*, 2, pp. 86-95, 1992.

[6] Fang, W. and Wickert, J.A., "Post buckling of micromachined beams," *J. Micromech. Microeng.*, **4**, pp. 116-122, 1994.
[7] Marshall, J.C., Read, D.T., and Gaitan, M., "Analysis of fixed-fixed beam test structures," *SPIE Microlithography and Metrology in Micromachining II*, SPIE Vol. 2880, pp. 46-55, Austin, Texas, 1996.
[8] Jensen, B.D., de Boer, M.P., and Miller, S.L., "IMaP: Interferometry for Material Property Measurement in MEMS," *1999 International Conference on Modeling and Simulation of Microsystems*, pp. 206-209, San Juan, Puerto Rico, 1999.
[9] Meng, Q., Mehregany, M., and Mullen, R.L., "Theoretical Modeling of Microfabricated Beams with Elastically Restrained Supports," *J. Microelectromechanical Systems*, **2**(3), pp. 128-137, September 1993.
[10] Gill, J.J.-Y., Ngo, L.V., Nelson, P.R., and Kim, C.-J., "Elimination of Extra Spring Effect at the Step-Up Anchor of Surface-Micromachined Structure," *J. Microelectromechanical Systems*, **7**(1), pp. 114-121, March 1998.